Capturing the complete landslide–debris-rich flood continuum for accurate inventory, susceptibility and exposure mapping – lessons from Cyclone Idai

Antoine Dille[1], Olivier Dewitte[1], Jente Broeckx[2], Koen Verbist[3], Andile Sindiso Dube[4], Jean Poesen[5,6], Matthias Vanmaercke[5]

[1] Royal Museum for Central Africa, Department of Earth Sciences, Tervuren Belgium
[2] Vlaamse Instelling voor Technologisch Onderzoek (VITO), Mol, Belgium
[3] UNESCO, Intergovernmental Hydrological Programme, Paris, France
[4] University College Cork, School of Biological, Earth & Environmental Sciences, Cork, Ireland.
[5] KU Leuven, Department of Earth and Environmental Sciences, Leuven, Belgium
[6] Maria-Curie Sklodowska University, Faculty of Earth Sciences and Spatial Management, Lublin, Poland

Correspondence to: Antoine Dille (antoine.dille@africamuseum.be)

Keywords: hazard interactions, cascading hazard, Cyclone Idai, data-scarcity, tropical cyclone, Africa, Zimbabwe

Abstract. In mountainous regions, intense rainfall can trigger thousands of landslides within hours. The drivers that control the occurrence of such landslides, and the methods for predicting the zones susceptible to their initiation have been extensively studied. Yet, for many of the most severe disasters associated with these landslide events, the main impacts on local communities occurred far from the source areas where most modelling efforts are focused. Sediments mobilized high on slopes by rainfall-triggered landslides can be transported many kilometres downstream, causing significant impacts along their path, while also feeding river systems with large amounts of sediments and consequently increasing flood risks. Such chain of cascading hazards significantly increases the destructive potential of landslides as well as their impact zone. Effective risk mitigation must therefore address not just susceptibility to initiation but also landslide mobility and hazard interactions—yet such studies remain rare.

With this work, we emphasize the importance of capturing what we refer to as the landslide–debris-rich flood continuum (landslide source, runout and related debris-rich floods) for accurate inventory, susceptibility and exposure mapping when landslide mobility is high – as it is often the case for extreme rainfall events. We apply this approach in two districts of eastern Zimbabwe (> 8000 km²), severely impacted by Cyclone Idai in March 2019. Using simple, replicable methods, we mapped over 14,000 (mostly) shallow landslides and 94 km² of debris-rich flood-affected zones. These data informed detailed susceptibility and exposure models that distinguish between the processes involved. Our results show that around 226,000 individuals live in areas of moderate to high susceptibility to landslide or debris-rich floods – closely matching official figures of those affected by the cyclone. Notably, landslide sources account for only about one-fifth of this total exposure. This highlights the need to consider the entire hazard continuum. Our approach also exemplifies how simple, open-access tools and data can be highly effective for hazard and risk analyses across of the globe.

1. Introduction

1.1. Context and objectives

Mountainous regions typically feature closely interconnected earth surface processes linked to hillslope material mobilization. These interactions increase the potential for cascading hazards, and consequently the overall risks faced by local communities (Gill and Malamud, 2014; Jacobs et al., 2016; Cutter, 2018; Tilloy et al., 2019; Gill et al., 2020; Lee et al., 2024; Yanites et al., 2025). Landslides are a striking example of this. Their most significant impact on populations and infrastructure often occurs not at the source, but through the transfer and deposition of the landslide material in downslope areas and channels where communities are commonly located (Mergili et al., 2018, 2019; Roback et al., 2018; Milledge et al., 2019). It is through this sequence of interconnected, sediment-transporting processes that many landslide events turn into disasters (Mergili et al., 2019; Wallace et al., 2022; Lee et al., 2024).

Two key factors determine the role of landslides in cascading hazards (Roback et al., 2018): (i) mobility, indicated by runout distance and volume (Legros, 2002; Iverson et al., 2015); and (ii) connectivity, or how much landslide material enters river channels (Wohl et al., 2019). Mobility – and destructive potential – is typically amplified by mixing hillslope material with large runoff volumes during intense rainfall and by erosion and entrainment of additional material like soils, rocks and, vegetation (Iverson and Ouyang, 2015; Pudasaini and Krautblatter, 2021). These mechanisms can turn landslides triggered high on hillslopes into high-mobility debris-rich flows that transport slope material several kilometres downstream from the source area (Iverson et al., 1997; McGuire et al., 2024) and ultimately contribute to the formation of debris-rich (flash) floods (Slater et al., 2015; Croissant et al., 2017; Bennett et al., 2025). Together, these cascading effects expand both the destructive potential and impact zones of the initial landslides (e.g., Jacobs et al., 2016).

Such a continuous sequence of linked sediment-gravity flows (landslides) and fluid-gravity flows (debris to water floods) exemplifies a chain of *cascading land hazards* – a topic that has received growing attention in recent literature (e.g., Tilloy et al., 2019; Brenna et al., 2020; Gill et al., 2020; Keck et al., 2024; Arango-Carmona et al., 2025; Yanites et al., 2025). The *cascading land hazards framework* (Yanites et al., 2025) broadly encompasses all linked chains of processes that move water and sediment across Earth's surface, in which one event directly influences the likelihood or intensity of another. This differs from compounding hazards, which refers to co-occurrence and amplification of events that are statistically independent (Yanites et al., 2025). Identifying and constraining such cascading chain of hazard is critical for comprehensive risk assessment (Gill and Malamud, 2014; Cutter, 2018; De Angeli et al., 2022). Although the importance of these interactions has long been recognized (e.g., van Westen et al., 2006), they remain underrepresented in hazard, risk and exposure assessments (Gill et al., 2020; Sharma et al., 2023; de Vilder et al., 2024). Despite growing landslide susceptibility research (e.g., Reichenbach et al., 2018; Merghadi et al., 2020), the vast majority of studies remain focused on landslide initiation, often overlooking mobility and cascading effects (Di Napoli et al., 2021). A number of exceptions exist (e.g., Kritikos and Davies, 2015; Fan et al., 2017; Melo et al., 2019; Mergili et al., 2019; Di Napoli et al., 2021; Van Den Bout et al., 2022; Zhou et al., 2022; Dubey et al., 2023; Keck et al., 2024), but they typically rely on complex and data-demanding models that constrain them to small-case studies (Fan et al., 2017; Mergili et al., 2019). Likewise, exposure mapping – i.e. the identification of populations and infrastructure at risk – remains a relatively underexplored dimension of (cascading) hazard research (Emberson et al., 2020; Lin et al., 2023).

Here, we demonstrate the value of explicitly considering the cascading chain of hazards encompassing landslides to debris-rich floods for inventory, susceptibility, and exposure mapping alongside extreme triggering events. We show the benefits of our approach in two districts of eastern Zimbabwe, severely impacted by Cyclone Idai in March 2019, where landslide and flood hazards data remain scarce. Using simple, replicable methods, we offer insights into this extreme event's consequences, producing comprehensive products to guide land use planning, mitigation, and risk reduction in the region.

1.2. The 2019 Cyclone Idai and its associated landslides in eastern Zimbabwe

Cyclone Idai (Fig. 1a) ranks among the deadliest storms ever recorded in the southern hemisphere (Devi, 2019). In March 2019, it caused widespread flooding across Mozambique, Malawi, and Zimbabwe, resulting in thousands of fatalities and affecting over three million people – many already in need of humanitarian assistance (Chatiza, 2019). In eastern Zimbabwe, the extreme rainfall (300–450 mm between 15–19 March– nearly half the region's annual average of ~1000 mm; IMERG-GPM satellite estimates (Huffman et al., 2019), see Fig. 1a) triggered thousands of highly mobile landslides that severely impacted mountain communities in the Chimanimani and Chipinge districts (e.g., Chatiza, 2019; Chanza et al., 2020).

Beyond human and infrastructural losses, the geomorphic impacts – ranging from sediment redistribution to disrupted ecosystem services – were substantial (Das and Wegmann, 2022). Most landslides consisted of shallow soil/regolith and debris slides/avalanches, typically initiating on steep, clay-rich, deeply weathered slopes (Das and Wegmann, 2022; see Fig. 1bc). These shallow landslides were often highly mobile, with the frequent transitions to debris flows. These flows carved clear debris trails from the hillslope into main river channels, with evident signs of material erosion and entrainment (Fig. 1b, 1c). Ultimately, they fed into sediment-laden floods that impacted communities tens of kilometres downstream (Fig. 1d). This cascading sequence – from landslide initiation to debris flows and sediment-rich floods – was central to the disaster's scale, highlighting the need to explicitly analyse such hazard chains for effective mitigation.

Our work focuses on the Chimanimani and Chipinge districts in eastern Zimbabwe, home to approximately 560,000 inhabitants (Zimbabwe National Statistics Agency, 2022) across ~8,600 km². These were the most severely affected districts in Zimbabwe, also hosting the majority of landslides triggered by Cyclone Idai. As in much of the Global South – and particularly in Africa – this region suffers from a lack of research on geo-hydrological hazards and risks (Broeckx et al., 2018; Dewitte et al., 2022).

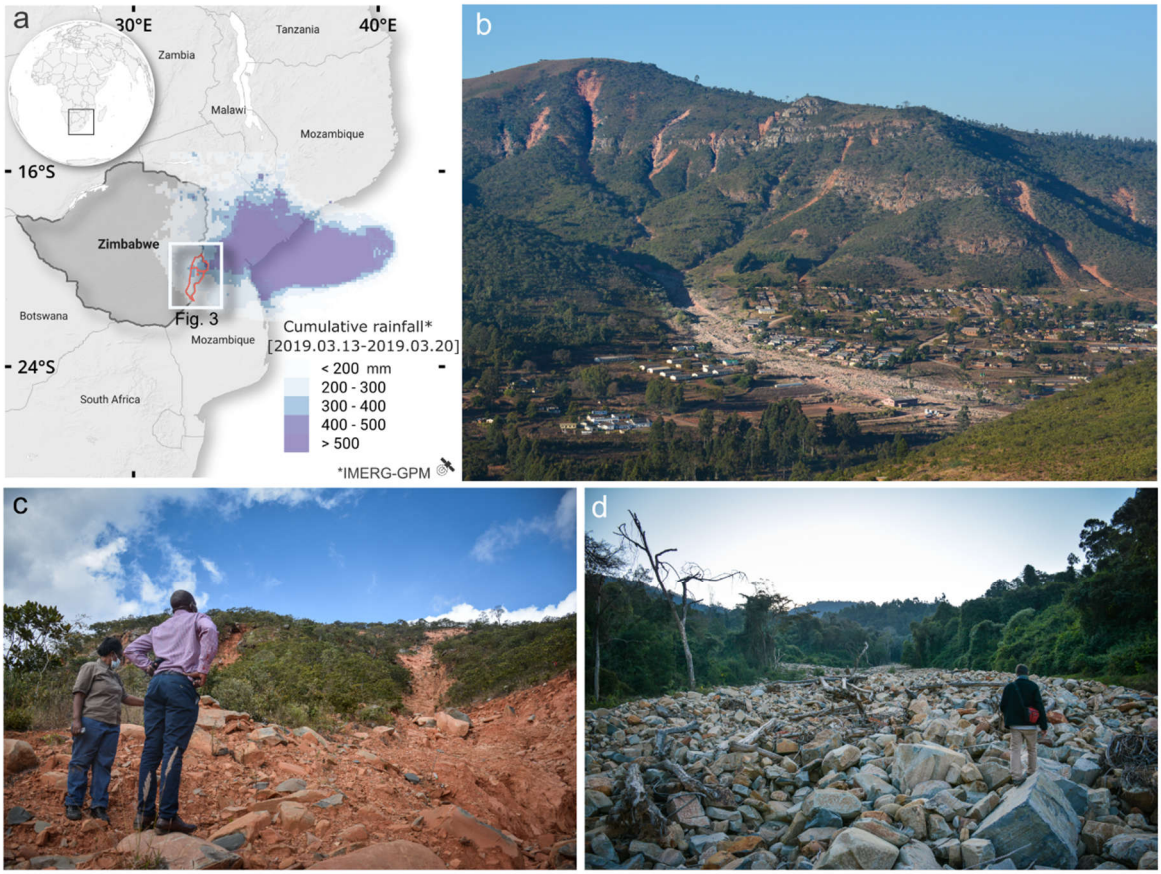

Fig. 1. Landslides and debris-rich flood triggered by Cyclone Idai in eastern Zimbabwe | a. Cumulative rainfall from March 13–20, 2019, estimated by IMERG-GPM satellite (0.1° × 0.1° resolution; (Huffman et al., 2019)). Focus districts in eastern Zimbabwe are highlighted in red. **b.** Highly mobile landslides triggered by Cyclone Idai near Ngangu Township, Chimanimani (July 2021), with **c.** zoom on their runout zones and **d.** related debris-rich flood deposits. Panel **b** shows clear debris trails from shallow landslides, with evidence of erosion and entrainment, particularly visible in panel **c**, which contributed to severe impacts in Chimanimani Town. Photos taken ~2.5 years after the event (© M. Vanmaercke).

1.3 Introducing the concept of landslide – debris-rich flood continuum

The *cascading land hazards* framework is intentionally broad (Yanites et al., 2025). To more precisely describe the tightly coupled and progressive sequence of sediment-transporting phenomena observed alongside Idai, we introduce the concept of the *landslide–debris-rich flood continuum*. We distinguish three interconnected stages, marked by decreasing sediment-to-water ratios: landslide source, runout, and debris-rich flood (Fig. 2). While these stages typically occur successively along topographic profiles, their boundaries remain porous in terms of process classification – potentially encompassing a range of mass movement types, including shallow soil and debris slides, debris avalanches, debris flows, hyperconcentrated flows, debris floods, and (debris-rich) (flash) floods (e.g., Hungr et al., 2014; Church and Jakob, 2020). The landslide source refers to the failure zone, where material detaches from the slope. Runout zones are typically channelized paths where entrainment and deposition occur, often influenced by runoff and/or the merging of multiple slope failures. Finally, *debris-rich floods* involve water-dominated flows in high order channels, but that are capable of transporting slope material far beyond the immediate vicinity of the landslides and their runout (Fig. 2).

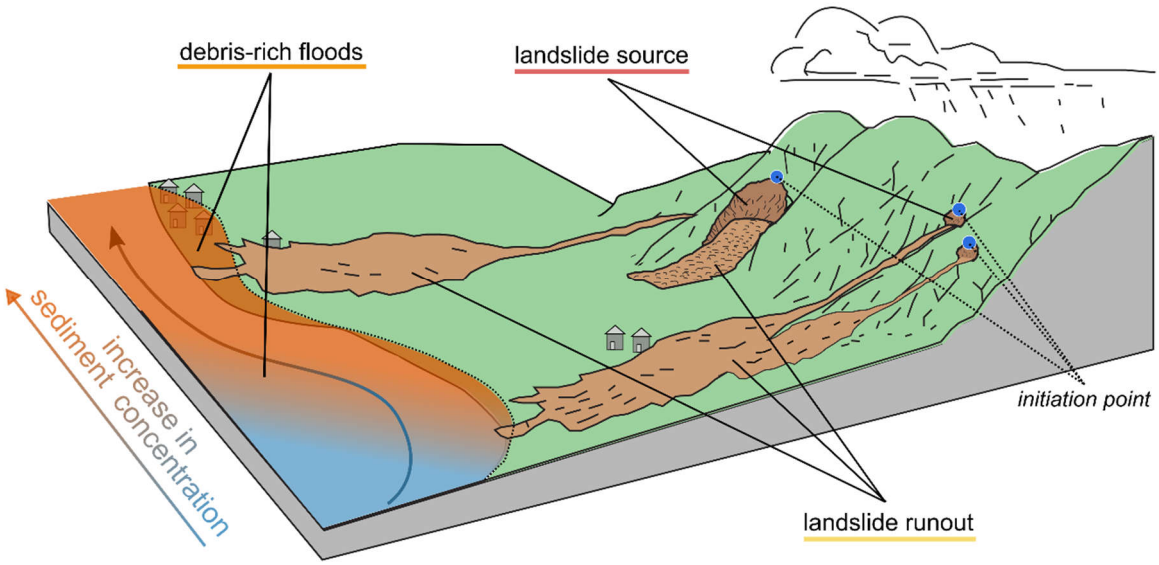

Fig. 2. | Illustration and definition of the landslide–debris-rich flood continuum, showing landslide source, landslide runout, and associated debris-rich flood zones as mapped in this study. Locations of the initiation points used during the manual inventory (*INV_02-POINT*) are also indicated. Adapted from Highland and Bobrowsky (2008).

2. Data and methods

2.1 Mapping the zones affected by Idai

We followed a three-step methodology to map and classify the areas affected by Cyclone Idai. First, we manually mapped parts of the two districts to build a reference inventory for training and validation. Second, we automatically identified all the zones impacted based on satellite images. Third, we classified these zones according to the process at play (i.e., landslide source, runout, or debris-rich flood).

2.1.1 Step 1: manual mapping for model training and validation ***(INV_01-POLY, INV_02-POINT)***

We first created two manually mapped datasets to train and validate subsequent products. **INV_01-POLY** consists of a detailed classification of affected and unaffected zones over ~1,300 km² (~15% of the study area), using 3-m resolution PlanetScope imagery from late March–early April 2019 (Fig. 3a). We mapped 1,240 landslide source zones (2.3 km²; avg. size 1,860 m²), 200 runout zones (3.3 km²; avg. size 16,700 m²), and 54 debris-rich flood deposits (27 km²; avg. size 482,000 m²), along with ~1265 km² of unaffected areas. **INV_02-POINT** is a point dataset of ~14,900 landslide initiation points across the full study area, digitized using very-high-resolution Google Earth imagery (April 2019–June 2021), with points placed at the headscarp of each landslide (see Fig. 2; Fig. 3b).

2.1.2 Step 2: automatic detection of affected zones

We compared Normalized Difference Vegetation Index (NDVI) on pre- and post-event Sentinel-2 satellite images to map impacted areas. This simple metric proved sufficient for accurate delineation as the affected zones had a clear visual and spectral signature immediately following the events. To perform this analysis, we used the open-source HazMapper application (Scheip and Wegmann, 2021) in Google Earth Engine, which generates "greenest-pixel" composites over one-month periods before and after mid-March 2019. This approach reduces the influence of clouds and phenological variability by retaining only the highest NDVI value per pixel within the time window.

The resulting NDVI gain/loss maps, produced at a 10-m resolution (Sentinel-2 resolution), were compared with **INV_01-POLY** to determine an optimal threshold for delineating impacted areas. Six

NDVI thresholds (from –8% to –18%) were tested; a threshold of –12% yielded the best performance, correctly identifying 97% of mapped landslide source, runout, and debris-rich flood zones, with omission and commission errors of 0.55% and 2.6%, respectively. The small omission error indicates that nearly all impacted areas were captured, while the slightly higher commission error was primarily due to unrelated deforestation activities occurring within the one-month analysis window. These false positives, which had a typical signature, were manually removed.

2.1.3 Step 3: classification of affected zones ***(INV_03-AUTO)***

We developed a multinomial logistic regression model to classify the automatically detected impacted zones into three process types: landslide source, runout, and debris-rich flood (**INV_03-AUTO**; see Fig. 2, Fig. 3c). The model, implemented in Python using the *Scikit-learn* library (Pedregosa et al., 2011), was trained on the **INV_01-POLY** dataset using a cross-entropy loss function. To address class imbalance (e.g., the larger spatial extent of debris-rich flood deposits), we applied the Synthetic Minority Oversampling Technique (SMOTE) to oversample minority classes and downsample the majority class. 70% of the mapped pixels were used for training and 30% for testing.

To differentiate between the various processes occurring along the slope profile, we selected predictors that capture where mass is likely to be mobilized, transported, or deposited. These are primarily topographic factors that reflect slope geometry, drainage, and terrain position. Predictors for the model were derived from the Copernicus GLO-30 digital elevation model (DEM, see Table 1) but we do not expect large differences in end-results with other DEMs of similar resolution and accuracy. Specifically we used: i) **local downward relief** (calculated within a 200 m radius); ii) **topographic wetness index** (TWI); iii) **topographic position index** (TPI) over 300 m radius (Weiss, 2001); iv) **normalized steepness index** (Ksn), capturing slope and upstream contributing area characteristics (Vanmaercke et al., 2020); v) **flow accumulation**, weighted by a continental landslide susceptibility map (Broeckx et al., 2018) to give more importance to drainage paths likely to receive material from upslope failures; and vi) **forest cover** and **forest loss (2014-2018)** from Hansen et al. (2013), reflecting vegetation-related controls on slope stability in tropical regions (e.g., Depicker et al., 2021a, 2021b). All predictors were normalized (mean-centered and scaled by standard deviation) and calculated at original 30-m DEM resolution. The classification was performed with upsampled predictors to exploit the 10-m resolution map of impacted zones derived from Sentinel-2 data.

To address potential multicollinearity among predictors, we applied a three-step procedure: (1) Pearson correlation analysis to flag variable pairs with $|r| > 0.8$, (2) Variance Inflation Factor (VIF) computation to identify variables with $VIF > 10$, and (3) iterative removal of highly collinear variables based on both criteria. Model performance was then compared across three feature sets: i) all predictors, ii) predictors with collinear variables removed, and iii) the top-5 features from univariate tests. As the full predictor set delivered the highest test accuracy, all variables were retained for final model training and susceptibility mapping.

Table 1. | Landslide predictors used in the logistic regression models for both inventory classification (Section 2.1.3) and susceptibility analyses (Section 2.2), grouped by theme following Reichenbach et al. (2018). *Note: HazMapper NDVI loss* was used only for the classification model, see section 2.2 .*

theme	predictor variables	units	original resolution	source
Morphology	Slope	m/m	30 m	Copernicus DEM
	Upslope Curvature	rad.m-1	30 m	Copernicus DEM
	Local Downward Relief	m	30 m	Copernicus DEM
	Mean Local Relief	m	30 m	Copernicus DEM
Hydrology	Distance to River	m	30 m	Copernicus DEM
	Fl. Acc weighted by landslide susceptibility		30 m	Copernicus DEM + Broeckx at al. 2018
	Topographic Wetness Index (TWI)		30 m	Copernicus DEM
	Topographic Position Index (TPI)		30 m	Copernicus DEM
	K_{sn}	m0.3	30 m	Copernicus DEM
Landcover	Forest Cover		30 m	Hansen et al., 2013
	Forest Loss [2014 - 2018]		30 m	Hansen et al., 2013
Idai impact zones*	*HazMapper NDVI loss**		*10 m*	*Sentinel-2*

Model performance was evaluated using receiver operating characteristic (ROC) curves, precision–recall curves, and prediction rate curves. ROC curves quantify the ability to separate classes through the area under the curve (AUC), while precision–recall curves provide complementary insight, being more sensitive to omission errors (i.e., false negatives), offering additional information on class-wise prediction accuracy. Prediction rate curves were also used, given their relevance for assessing the spatial predictive power of susceptibility models (e.g., Zêzere et al., 2017). They illustrate the proportion of landslides expected to fall within a given susceptibility class, thereby providing an actual measure of the model's success rate.

To assess the role of individual predictors, we also trained univariate models and computed ROC_{uni} scores, averaged over 10-fold cross-validation (Depicker et al., 2020), with higher values reflecting stronger class discrimination. Additionally, the influence of predictors in the multivariate model was quantified using odds ratios (OR), derived from the three process models and calculated with 10-fold cross-validation. Finally, model stability was tested through repeated cross-validation using the full set of predictors, revealing minimal coefficient variability (<1%), suggesting robust model performance.

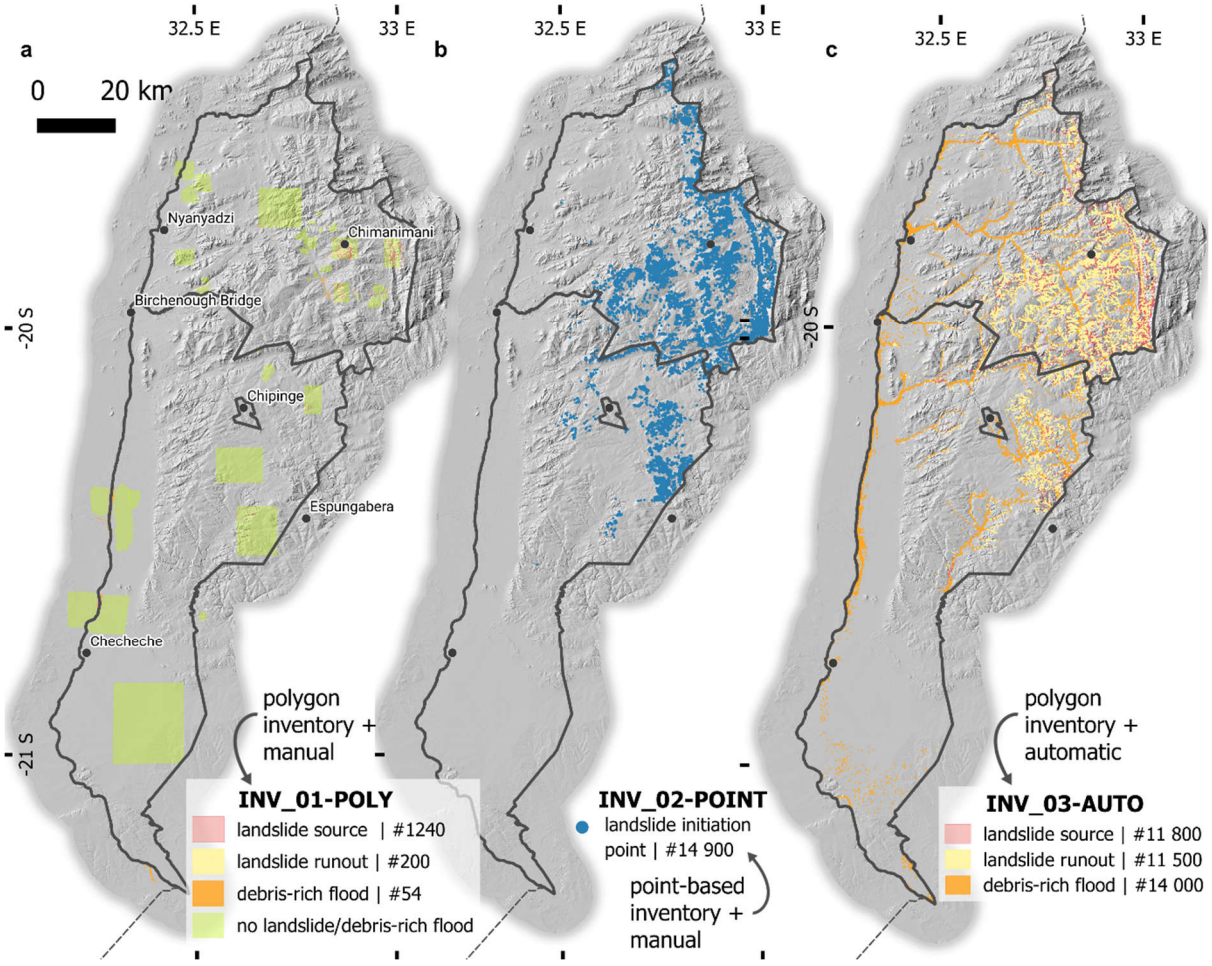

Fig. 3. Inventory and classification of landslide source, runout and debris-rich flood. | a. Manual polygon-based inventory (**INV_01-POLY**) of parts of the two districts, used for training and validating the logistic regression model (cf. sections 2.1.3 and 2.2). **b.** Manual inventory of landslides initiation points triggered by Idai across the entire two districts (**INV_02-POINT**), with each point representing a single landslide. **c.** Automatic inventory of the classified impacted zones for the two entire districts (**INV_03-AUTO**).

2.2 Assessing the landscape susceptibility

We applied a similar modelling approach as in section 2.1.3 to assess the susceptibility of each pixel of the two districts to one of the three processes in the landslide – debris-rich flood continuum (or none). The logistic regression model uses the same environmental predictors as before (Table 1), except for the HazMapper-calculated NDVI loss, which was excluded to avoid overfitting to Idai event. Collinearity and feature-selection analyses were repeated, and ultimately all features were used. For interpretability and cross-model comparison, susceptibility values were classified into five categories: very low, low, moderate, high, and very high, following Stanley and Kirschbaum (2017). Each category contains twice as many pixels as the next highest, ensuring consistency across models and highlighting the most susceptible areas. In addition to accuracy metrics obtained from validation pixels from the manual polygon inventory (INV_01-POLY), we assessed model predictions against the automatically generated inventory of thousands of landslides and debris-rich floods from section 2.1.3 (INV_03-AUTO), which was not used for susceptibility model construction. This inventory provides a large, spatially unbiased dataset covering the entire study area (compared to the ~15% coverage by INV_01-POLY), though being built on a large-impact event may marginally reduce predictive performance for smaller, more isolated occurrences.Note that the debris-rich flood susceptibility model was restricted to mountainous areas, where sediment-laden flows are most likely; farther downstream, sediment

concentrations decrease and flash floods behave differently, making them harder to assess with our available data and approach. Flat areas, known to artificially inflate model performance (Brenning, 2012), were also excluded from the landslide source zone analysis.

2.3 Mapping the population and building exposure

Exposure assessment seeks to identify population and infrastructure at risk, in order to prioritize risk management and future mitigation efforts (Emberson et al., 2020; Dubey et al., 2023). This is achieved by intersecting the susceptibility with population distribution and building/infrastructure footprints. We produced exposure estimates for each of the three susceptibility models: landslide source, runout, and debris-rich flood (section 2.2). In terms of elements potentially at risk, we considered the population (density and individual buildings) and key infrastructure (roads, bridges, schools, health centres; Supplementary Fig. 1). For this, we combined (typically incomplete) OpenStreetMap building data with Facebook High Resolution Population Density Maps (30 × 30 m estimates; last updated 2022; Tiecke et al., 2017) and Google Open Buildings (individual footprints; last updated 2022; Sirko et al., 2021), retaining only buildings with >65% confidence. Infrastructure data were obtained from the UNESCO Regional Office for Southern Africa (mostly from digitized areal imagery) and combined with OpenStreetMap. Overlaying these datasets with susceptibility maps resulted in pixel-based exposure maps for both districts and classifications of exposure levels for individual buildings and infrastructure. Additionally, population and building data were compared to observed extent of Idai impacts to assess consistency between exposure estimates and figures reported by NGOs and government sources.

3. Results

3.1 Idai's impacts inventory

We identified 130 km² impacted by landslides and debris-rich floods (~1.5% of the total area of 8,600 km²; Fig. 4). Most landslides occurred in eastern Chimanimani, which is more mountainous and received higher rainfall totals (average 330 mm, with ~1,300 km² receiving >350 mm between 15–19 March 2019 based on satellite estimates). In contrast, rainfall over Chipinge averaged 230 mm, with no areas exceeding 330 mm (IMERG-GPM satellite estimates; Fig 5a).

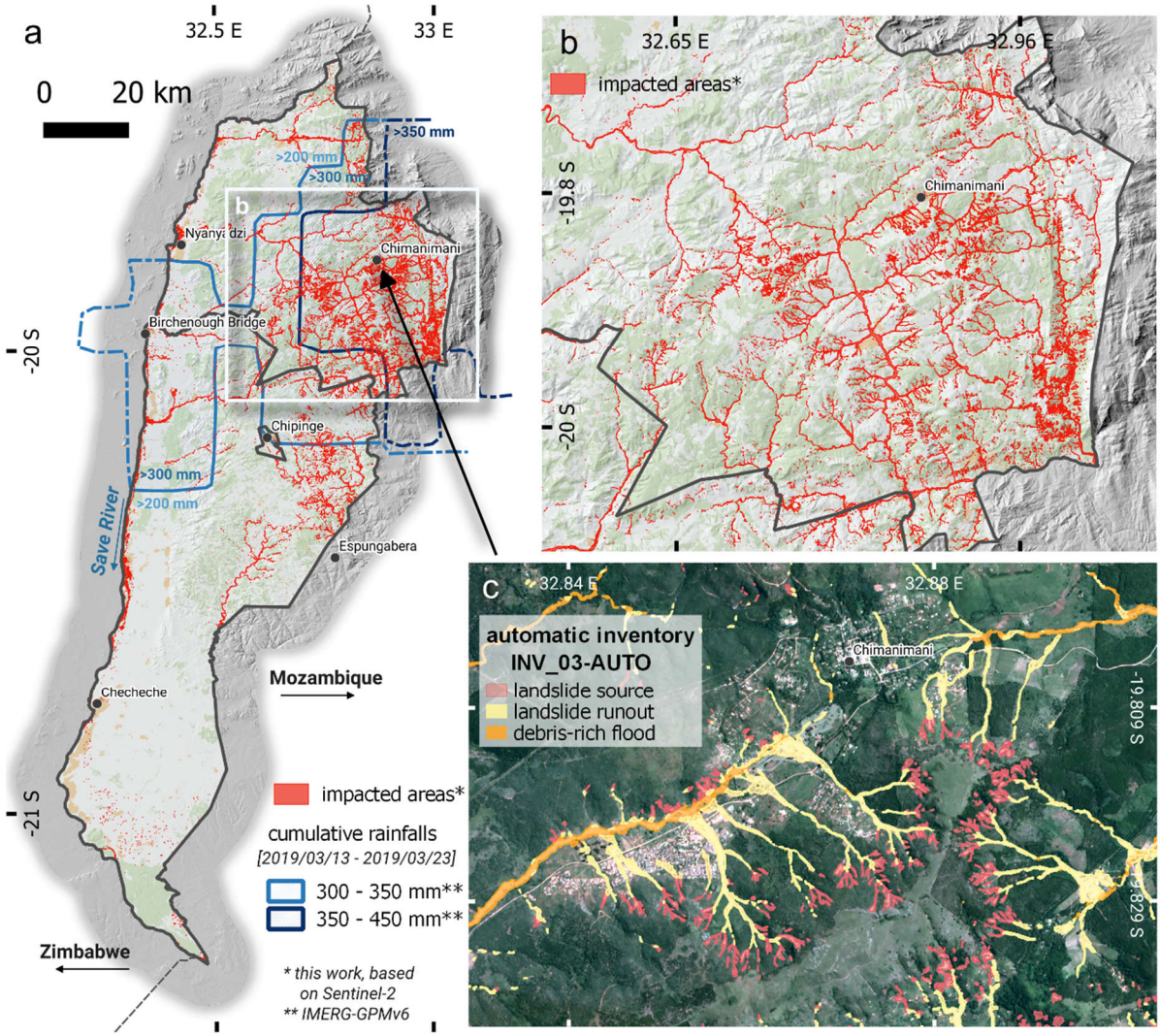

Fig. 4. Automatically detected impacted areas and classification (INV_03-AUTO). | a. Red zones indicates areas affected by landslides or debris-rich floods (i.e., zones where the vegetation has been damaged, removed and/or covered by sediments) alongside Idai for Chimanimani (North) and Chipinge (South) districts. These zones were identified by comparing of pre and post-event Sentinel-2 composites. Pale blue and dark blue contours show cumulative rainfall >300 and >350 mm (satellite estimates) from 13–20 March 2019; other areas received ≥200 mm. **b.** Zoom on impacted areas in Chimanimani district. Elongated shapes indicate debris-rich flood zones, while small features on upper hillslopes are landslides; long runouts often connect the two. **c.** Detailed zoom on Ngangu Township, Chimanimani, showing automatic classification of landslide source, runout, and debris-rich flood (**INV_03-AUTO**). Definitions of these zones are illustrated in Fig. 2.

Automatic classification (INV_03-AUTO, Fig. 4c) detected 11,800 landslide source areas (mean 1,450 m², median 600 m², total 17.3 km²), 11,500 runout areas (mean 1,500 m², median 500 m², total 17.1 km²), and 14,000 debris-rich flood areas (mean 6,700 m², median 800 m², total 94 km²). Most landslide-

affected zones are in Chimanimani (31 km², 91%), while debris-rich flood zones are more evenly distributed (51 km² vs. 43 km² in Chipinge), mainly along rivers draining high landslide-density areas. High landslide density areas are also typically associated with long runout zones, which channelled large sediment volumes from hillslopes into rivers.

The logistic regression classifier performed well, achieving validation AUCs of 0.90 for runout, 0.94 for source, and 0.97 for debris-rich floods. Adding HazMapper NDVI gain/loss as a predictor increased AUCs to 0.94–0.98, especially improving separation between runout and debris-rich flood classes. Precision–recall scores ranged from 0.73 (runout) to 0.91 (debris-rich floods), improving to 0.82–0.94 with HazMapper NDVI. Most misclassifications occurred between landslide source and runout classes. About 11,000 of the 14,900 manually inventoried landslide initiation points (*INV_02-POINT*) lie within 100 m of an automatic source area (73.8%, *INV_03-AUTO*). Automatic delineation also identified 21% fewer sources, reflecting both missed landslides and amalgamation of adjacent ones (Marc and Hovius, 2015).

Topographic variables were found key predictors (Table 2): slope for landslide source, susceptibility weighted flow accumulation for runout, and local downward relief plus topographic wetness index (TWI) for debris-rich floods. Though a weak predictor on its own, TWI was also an important (negative) predictor for source and runout zones. Forest cover (but not recent loss) had no individual predictive power yet contributed to multivariate models. Conversely, K_{sn} was a strong individual predictor for source and runout, but was less influential in the multivariate model.

Table 2. Predictor importance. | The relative importance of the predictors (Table 1) for modelling each process individually is assessed through comparison of univariate AUC ROC_{uni}. The odds ratios (OR) are derived from multivariate model and calculated with 10-fold cross-validation (CV).

landslide source			landslide runout			debris-rich flood		
predictor	**ROC_{uni}**	**OR**	**predictor**	**ROC_{uni}**	**OR**	**predictor**	**ROC_{uni}**	**OR**
Slope	0.87	2.65	Flow Acc. Weighted	0.93	2.02	Topo. Wetness Index	0.87	8.43
K_{SN}	0.87	1.04	K_{SN}	0.87	1.29	Local Downward relief	0.86	0.07
Mean Local Reflief	0.84	1.13	Upslope Curvature	0.85	0.48	Topo. Position Index	0.82	0.36
Local Downward relief	0.79	1.1	Topo. Position Index	0.84	0.62	Flow Acc. Weighted	0.81	1.86
Topo. Wetness Index	0.78	0.37	Distance to River	0.77	0.41	Upslope Curvature	0.81	1.36
Forest Cover	0.75	1.57	Forest Cover	0.67	1.4	Distance to River	0.75	0.54
Flow Acc. Weighted	0.74	1.13	Mean Local Reflief	0.58	0.53	Mean Local Reflief	0.7	1.19
Topo. Position Index	0.74	0.55	Slope	0.58	0.76	K_{SN}	0.7	1.2
Distance to River	0.59	0.59	Local Downward relief	0.5	1.12	Slope	0.68	5.43
Upslope Curvature	0.56	0.94	Forest loss ['14- '18]	0.5	1.11	Forest Cover	0.55	2.12
Forest loss ['14- '18]	0.5	0.97	Topo. Wetness Index	0.49	0.35	Forest loss ['14- '18]	0.5	1.05

3.2 Susceptibility

The susceptibility models for the three distinct processes (Figs. 5 and 6) highlight how different hazards clearly affect specific landscape zones. A clear gradient emerges with altitude and slope, shaping the susceptibility to landslide sources, landslide runout, and debris-rich floods. Prediction rate curves indicate that, over an unspecified time frame, 83% of future runout zones are expected to fall within the 20% of the study area identified as most susceptible. Predictive accuracy is even higher for landslide sources (87%) and debris-rich floods (95%).

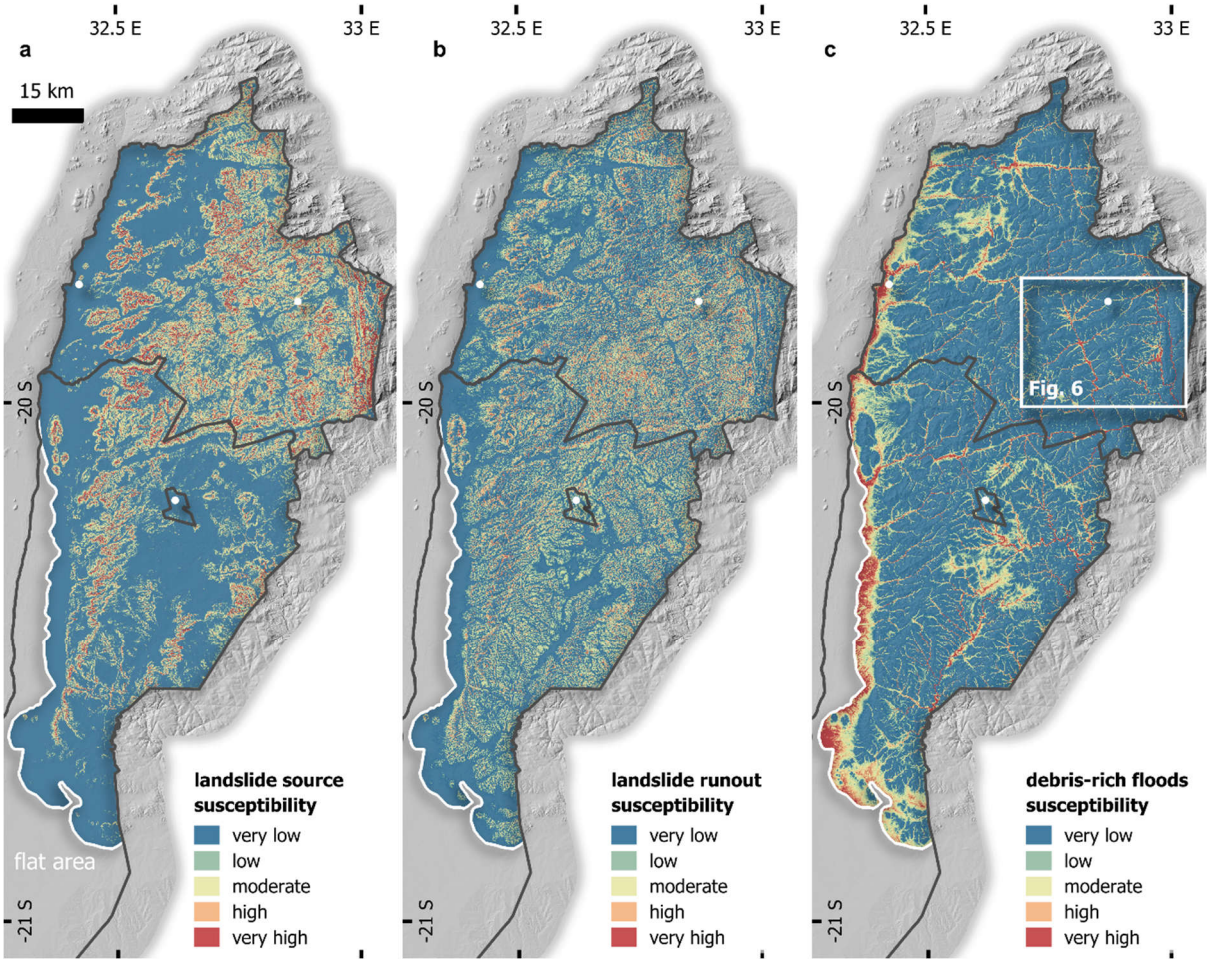

330

Figure 5. Susceptibility maps. | Maps showing susceptibility to **a.** landslide source, **b.** landslide runout and **c.** debris-rich flood in Chimanimani and Chipinge districts.

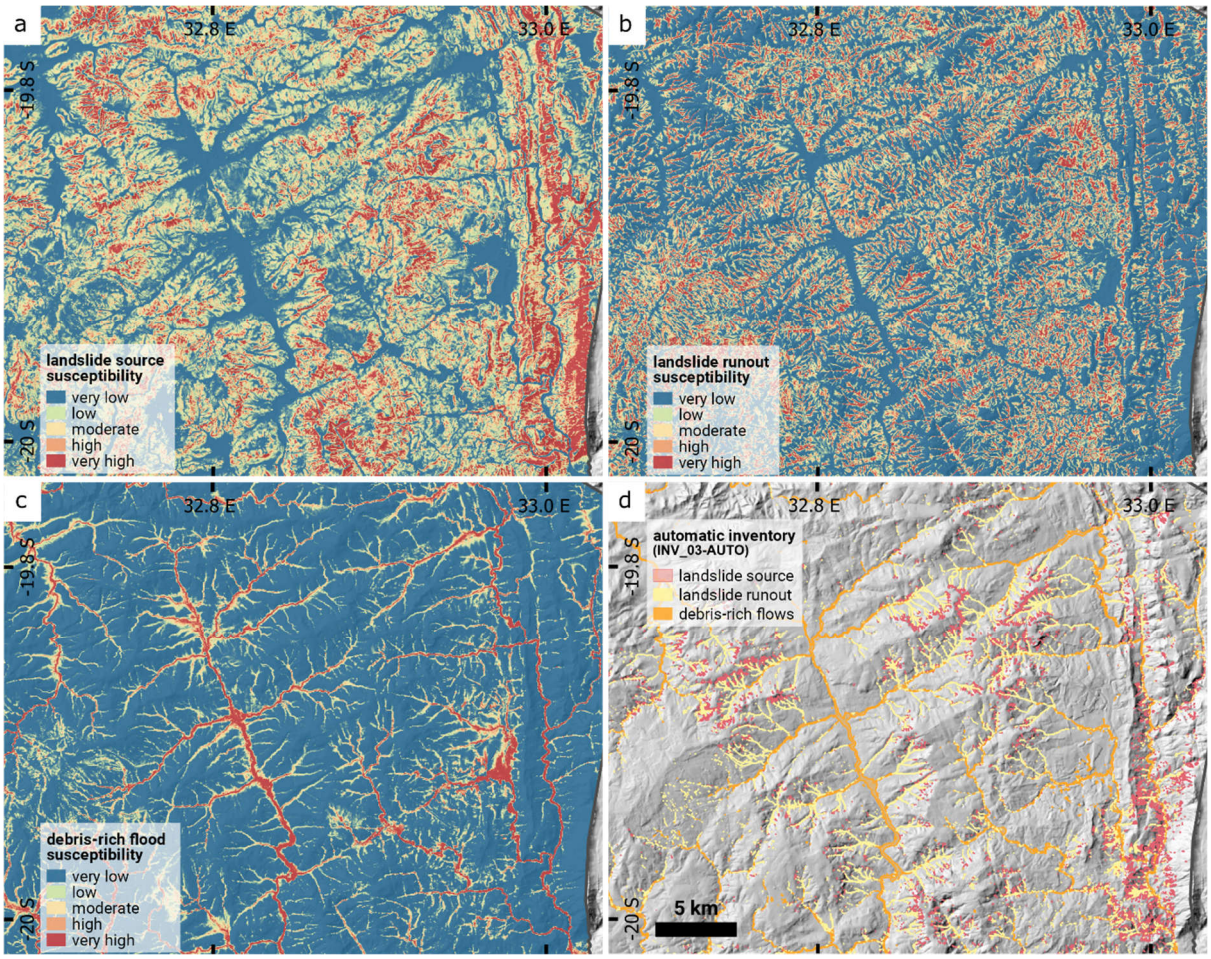

Fig. 6. Susceptibility maps – zoom on Chimanimani. | Maps showing susceptibility to being a **a.** landslide source area, **b.** landslide runout zone and **c.** debris-rich flood zone. **d.** Automatic inventory (INV_03-AUTO) of landslides and debris-rich floods in the same area. The extent of the area shown here is indicated in **Fig. 5c.**

3.3 Exposure

Many settlements in the two districts exhibit high exposure (Fig. 7), with an uneven spatial distribution of the population creating notable contrasts between susceptibility and exposure maps. Importantly, these figures highlight significant discrepancies in exposure to the three processes around the landscape. As expected, areas with the highest exposure to landslides and runout are predominantly located in the mountainous regions. In contrast, areas west of the two districts, along the main streams, show high population and building exposure to debris-rich floods.

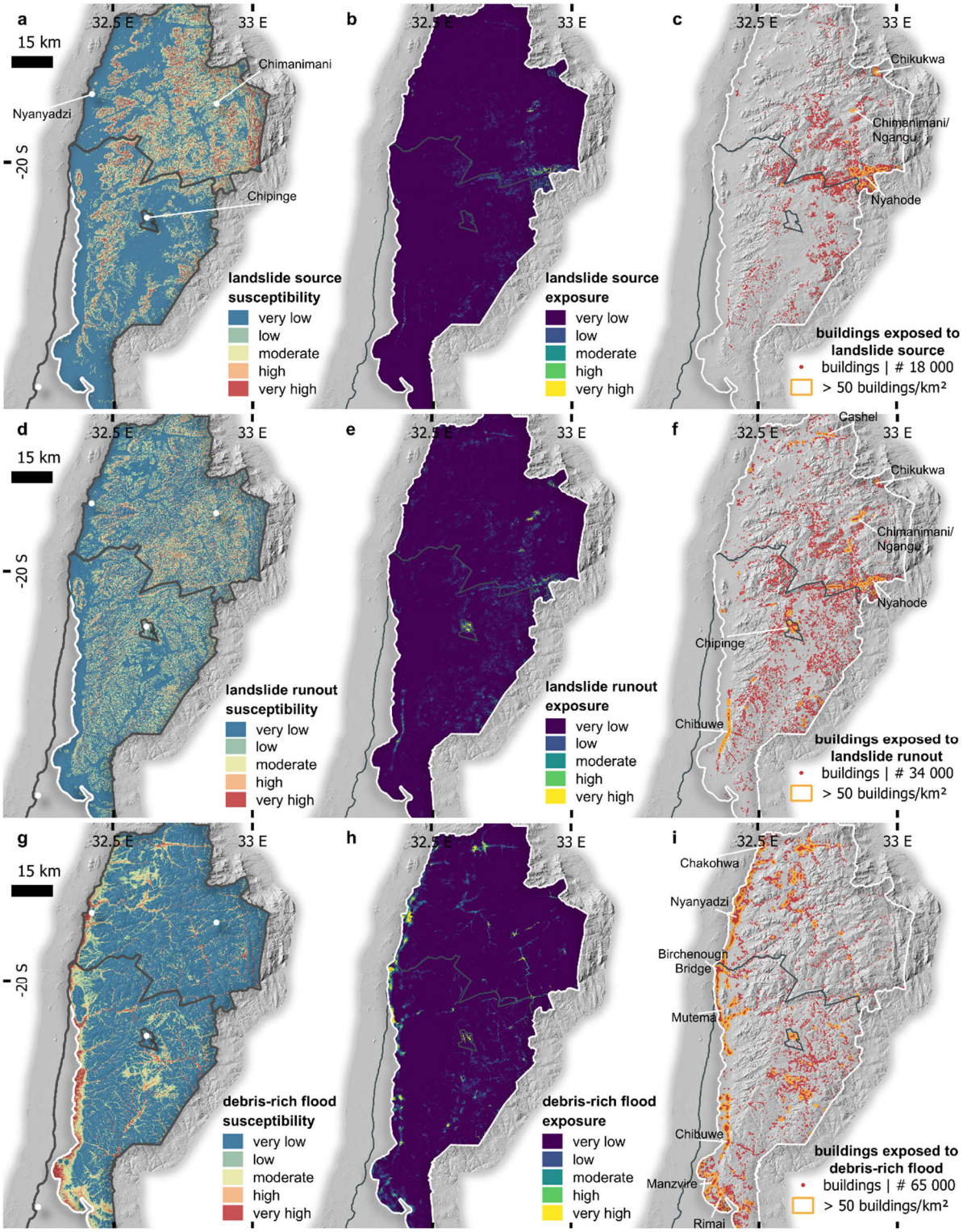

Fig. 7. Susceptibility and exposure levels. | Susceptibility, population and building exposure to **a-c.** landslide source, **d-f.** landslide runout, **g-i.** debris-rich flood. Hotspots of building exposure (> 50 buildings/km²) are circled in orange. # indicates estimates of the number of buildings in moderate to very high exposure zones. Colour scales are comparable across the susceptibility and exposure maps.

Because most people settle in relatively flat areas near streams and floodplains, much more individuals and buildings are exposed to landslide runout and debris-rich flood than to landslide sources (Table 3a). Overall, 29% of the population (~120,000 people) and 30% of buildings (~65,000) lie in zones with moderate to very high susceptibility to debris-rich floods, which account for only 11% of the study area. For landslide runout, the exposed share is lower, with 17% of the population and 16% of buildings

within susceptible zones covering 9.6% of the area. Exposure is lowest for landslide source susceptibility, where 9% of the population and 8% of buildings are located in zones covering 9.7% of the study area. Intersecting our detailed polygon inventory (INV_03-AUTO) with the mapped affected areas (Fig. 4a,b) further shows that about 23,000 buildings and 48,000 people—roughly 8% of all buildings and 8.5% of the population in Chimanimani and Chipinge districts (Zimbabwe National Statistics Agency, 2022) – are located within 100 meters of affected areas (Table 3b). Exposure of key infrastructures is substantial, with at least 60% for each type located in moderate or higher susceptibility zones – higher percentage than that of all buildings. Details and breakdowns by infrastructure type are provided in Supplementary Material.

Table 3. Estimating exposure of buildings and population. | a. Distribution of the number of buildings in the different susceptibility classes. The total number of buildings (Google Open Buildings, last updated in 2022; Sirko et al., 2021) and people (Facebook High Resolution Population Density Maps, last updated in 2022; Tiecke et al., 2017) located in moderate to very-high susceptibility areas is also provided. **b.** Number of buildings and people in a zone affected by landslide source, runout or debris-rich flood alongside Idai in March 2019.

a. buildings in susceptibility class	**Landslide source**	**Landslide runout**	**Debris-rich flood**
very low	156200 | 72%	130900 | 60%	86600 | 40%
low	42600 | 20%	51300 | 24%	65000 | 30%
moderate	13100 | 6%	21900 | 10%	32700 | 15%
high	4300 | 2%	10900 | 5%	26500 | 12%
very high	300 | 0%	1500 | 1%	5700 | 3%
Buildings *in moderate to very high classes (total = 117 000 | 54%)*	18000 | 8%	34000 | 16%	65000 | 30%
Population *in moderate to very high classes (total = 226 000 | 43%))*	36000 | 9%	70000 | 17%	120000 | 29%
b. buildings and population nearby a zone affected by Idai (% of all buildings/population)			
Buildings within 100 m *of affected zone*	3700 | 1.3%	7300 | 2.5%	11700| 4.3%
Population within 100 m *of affected zone*	7300 | 1.3%	16400 | 2.9%	24300| 5.3%

4. Discussion

We mapped 130 km² (1.5% of the two districts) as being directly affected by landslides or debris-rich floods, with 14,900 individual landslide initiation points – remarkably high for a single event (e.g., see Emberson et al. (2022)). The severity of the impacts triggered by Idai (see section 1.2 and e.g., Chatiza, 2019; Devi, 2019) reflects both the region's high population density and vulnerability, and the cascading chain of processes we described as the landslide–debris-rich flood continuum.

Our estimates suggest that ~226,000 people live in areas of moderate to high susceptibility to landslides and debris-rich floods (Table 3a) – nearly half the district population. These numbers closely match official figures of individuals affected by Idai (192,000–270,000; Chatiza, 2019; IFRC, 2020). Notably, exposure to landslide sources account for less than one-fifth of total exposed people and buildings, while landslide runouts affect about twice as many, and debris-rich floods over three times as many (**Table 3)**. This pattern results from the concentration of settlements along gently sloping, higher-order channels prone to landslide runout and flooding (Mergili et al., 2018, 2019; Roback et al., 2018; Milledge et al., 2019), and underlines a critical point: effective risk reduction demands accounting for the entire landslide–debris-rich flood continuum.

Our work illustrates how large parts of a landscape can have low likelihoods of landslide initiation but can nonetheless be very exposed to landslide-derived material, particularly during rare but extreme events. Yet, most landslide inventories, susceptibility or exposure assessments still focus only on landslide initiation (Reichenbach et al., 2018; Milledge et al., 2019; Emberson et al., 2022), introducing major uncertainties in estimates of landslide frequency, size, and overall hazard and risk (van Westen et al., 2006; Tanyaş et al., 2017; Emberson et al., 2022; Bhuyan et al., 2025). Likewise, highly mobile landslides can deliver substantial sediment loads, amplifying both immediate and delayed flood risk (Slater et al., 2015; Croissant et al., 2017; Bennett et al., 2025). This highlights the need to integrate geomorphological hazards into flood risk evaluation (Slater et al., 2015; Brenna et al., 2023).

The sequence of processes at hillslope level – landslides on steep mountain ridges, runouts in flow accumulation zones directly downslope, and debris-rich floods in low-relief, high topographic wetness areas – nevertheless enables the development of simple yet accurate statistical models using only a few and easy to obtain topographic predictors. Accuracy assessment attests high accuracy in identifying affected areas, classifying process stages, and estimating susceptibility and exposure. Most confusion occurs between landslide source and runout, which is expected since these stages belong to the same process where sediment scouring and deposition may follow one another and for which even manual delineation is complex. Because all three stages share similar spectral signatures but occur at distinct locations along the hillslope, topographic predictors proved decisive. Expectedly (e.g., Milledge et al., 2019; Emberson et al., 2022), slope, local downward relief and topographic wetness index emerged as strong predictors (Table 2), with the last two indicating where landslide-derived sediments tend to accumulate. Weighted flow accumulation was likewise a key predictor of runout, primarily highlighting channels draining susceptible slopes. It is already effective despite the coarse susceptibility model used for weighting, and its performance could likely be improved by incorporating regional or landslide source-specific models. By contrast, neither deforestation nor forest cover had a significant role in predicting sources or runouts (e.g. (Maki Mateso et al., 2023), suggesting limited land-cover influence on landslide occurrence; at least in the case of Idai. Similar patterns are reported for other extreme rainfall-triggered (e.g., Marc et al., 2018) or earthquake-triggered landslide events (e.g., Wenchuan; Fan et al., 2018), and major flash floods (Merz et al., 2021), where trigger magnitude and distribution outweigh land-use effects. Finally, while more advanced approaches (e.g., object-based mapping such as ALADIM; Deprez et al., 2022) or physically-based models of landslide runouts (e.g., Mergili et al., 2019; Wallace et al., 2022; Keck et al., 2024) may provide incremental gains, our simple workflow delivers fast, flexible, and transparent results – a crucial advantage for both researchers and decision-makers (Amatya et al., 2023; Dahal and Lombardo, 2023). The design of the model around simple morphological and hydrological variables available globally also favours its replicability in other data-scarce regions.

The cascading chain of hazard triggered by Cyclone Idai is not unique. Yet, as long as risk management strategies continue to focus on isolated hazards rather than their cascading effects, human and natural systems will remain vulnerable to interacting processes (Gill et al., 2020; Sharma et al., 2023) responsible for some of the world's most devastating disasters (Mergili et al., 2019; Wallace et al., 2022; Lee et al., 2024). This may also help explain why disaster risk reduction policies often appear ineffective (Nohrstedt et al., 2021). This challenge is particularly acute in tropical mountain regions, where cascading processes are frequent and rural communities highly vulnerable – especially in underreported areas such as Africa (Dewitte et al., 2021; Sekajugo et al., 2024; Arango-Carmona et al., 2025).

5. Conclusion

This study provides a strong reminder of the need to move beyond a narrow focus on landslide initiation and to account for the entire landslide–debris-rich flood continuum for effective risk mitigation, particularly in the context of extreme climatic events like Cyclone Idai. Using simple and replicable methods, we mapped over 14,000 landslides and developed susceptibility and exposure models for two districts in eastern Zimbabwe. We estimate that ~226,000 people live in areas of moderate to high susceptibility, closely matching official figures of those affected by Cyclone Idai. Crucially, in the two districts, the main impacts on local communities often occurred far downstream from the landslide initiation areas, with sediment transfer via high-mobility landslides and debris-rich floods significantly amplifying the destructive potential and impact zones.

Our assessment shows that landslide initiation alone accounts for just one-fifth of the total exposure, underscoring the need to consider not only initiation but also subsequent mass movement and flood processes for accurate hazard and exposure assessment. Moreover, since runout and debris-rich flood zones are strongly controlled by flow accumulation and river patterns (weighted by susceptibility), they can be predicted with reasonable precision at the regional scale using limited input data. Overall, our findings demonstrate that integrating the concept of landslide–debris-rich flood continuum into hazard assessments is essential for effective mitigation but also relatively straightforward. We also show that, even in data-poor regions, simple approaches based on open-access tools and datasets can yield valuable, actionable insights.

Beyond the fundamental scientific contribution, this study was designed from the outset with disaster risk management in mind. The resulting landslide hazard and exposure maps developed for this extreme event directly informed practice: by identifying critical educational and health institutions at risk, they enabled a targeted multi-hazard analysis of 15 schools in the region, ultimately producing individual risk profiles and actionable investment criteria (UNESCO Intergovernmental Hydrological Program, 2021). This illustrates how such an approach can translate into concrete risk reduction measures, offering a replicable path for other disaster-prone regions across the Global South.

6. Datasets

The landslide and debris-rich flood inventories, susceptibility and exposure maps, and location of buildings in moderate to high exposure maps are available for download from UNESCO IHP Water Information Network System https://doi.org/10.63253/nii4g2ac. Sentinel data are made available by ESA through e.g. the Copernicus Data Space Ecosystem. All computer codes used in this work are available from the authors upon reasonable request.

7. Author contribution

A.D, M.V and O.D. conceived the study; A.D. processed and analysed the data and created the figures. A.D. wrote the manuscript, with main inputs from O.D., M.V., and J.P.; M.V., K.V. and A.S.D. participated in the field campaign. J.B. created the point-based landslide inventory. K.V. coordinated the BE-RESILIENT project. All the authors contributed to the final version of the paper.

Competing interests

At least one of the (co-)authors is a member of the editorial board of Natural Hazards and Earth System Sciences.

8. Acknowledgments

This work was carried out within the framework of the UNESCO project BE-RESILIENT Zimbabwe, funded by the World Bank and managed by the UNOPS Zimbabwe Idai Recovery Project. We also acknowledge support from BELSPO STEREO-IV LACTOSE project. The authors thank the local authorities who facilitated data collection and fieldwork in eastern Zimbabwe.

Appendix A.

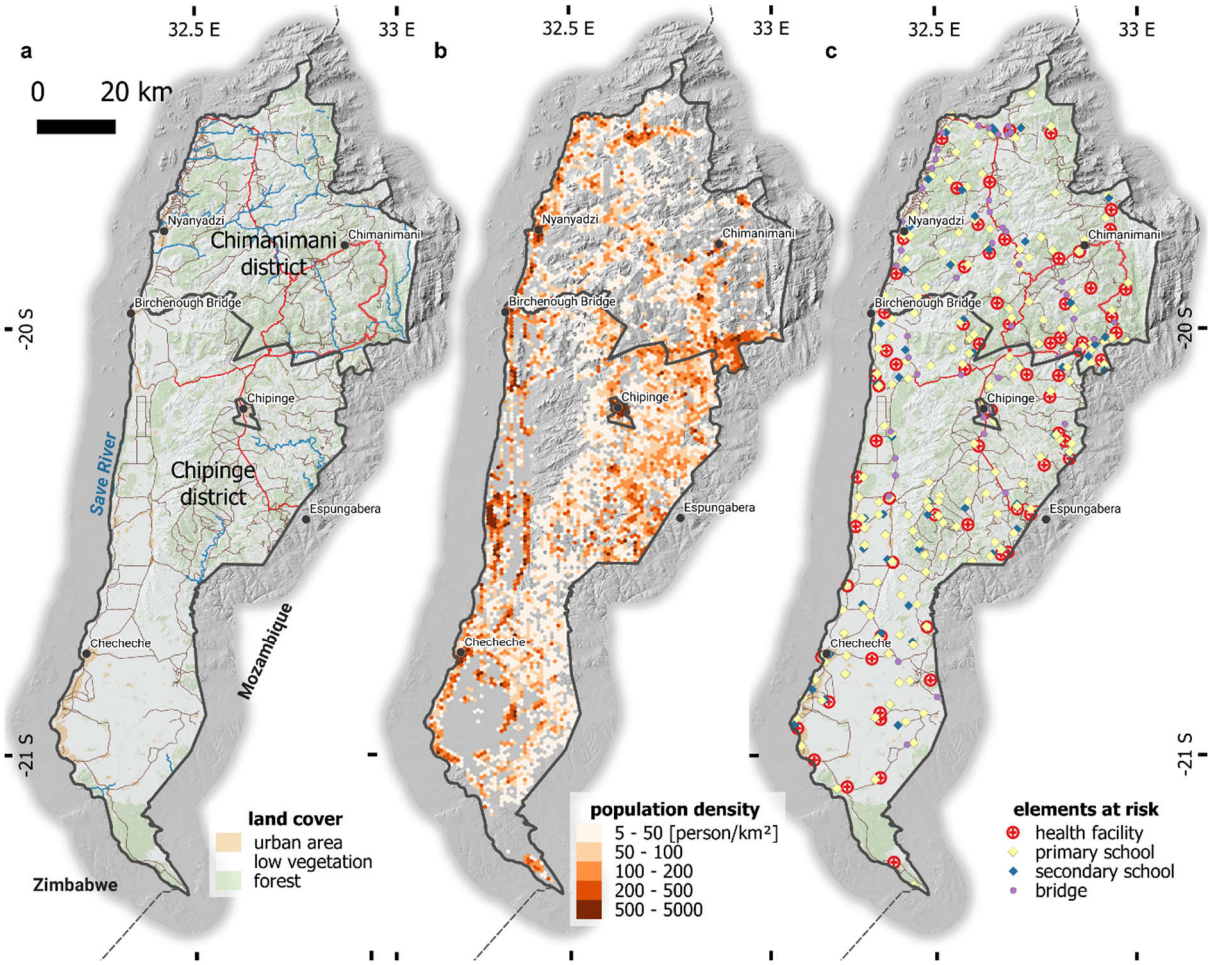

Fig. A1. Land cover, population density and key infrastructure in Chimanimani and Chipinge districts. | These layers were used to calculate the population and infrastructure exposure to landslide and debris-rich flood. Land cover: © ESA; population: © Facebook High Resolution Population Density Maps; key infrastructure: © UNESCO and © OpenStreetMap contributors 2024. Distributed under the Open Data Commons Open Database License (ODbL) v1.0.

Analysis of the exposure of key infrastructures (***Supplementary* Fig. *2***), shows that a minimum of 60% of all the infrastructure per type are located in zones with moderate or higher susceptibility to landslides and debris-rich floods. Only 14 (out of 188) bridges are located in zones with low susceptibility to landslide runout or debris rich floods. It is 22 (out of 61) for health facilities, 56 (out of 150) for primary schools and 19 (out of 48) for secondary schools for the three processes. It is also noteworthy that in zones of moderate to very high susceptibility, the proportion of key infrastructure at risk, including schools, health facilities, and bridges, is higher than that of all buildings.

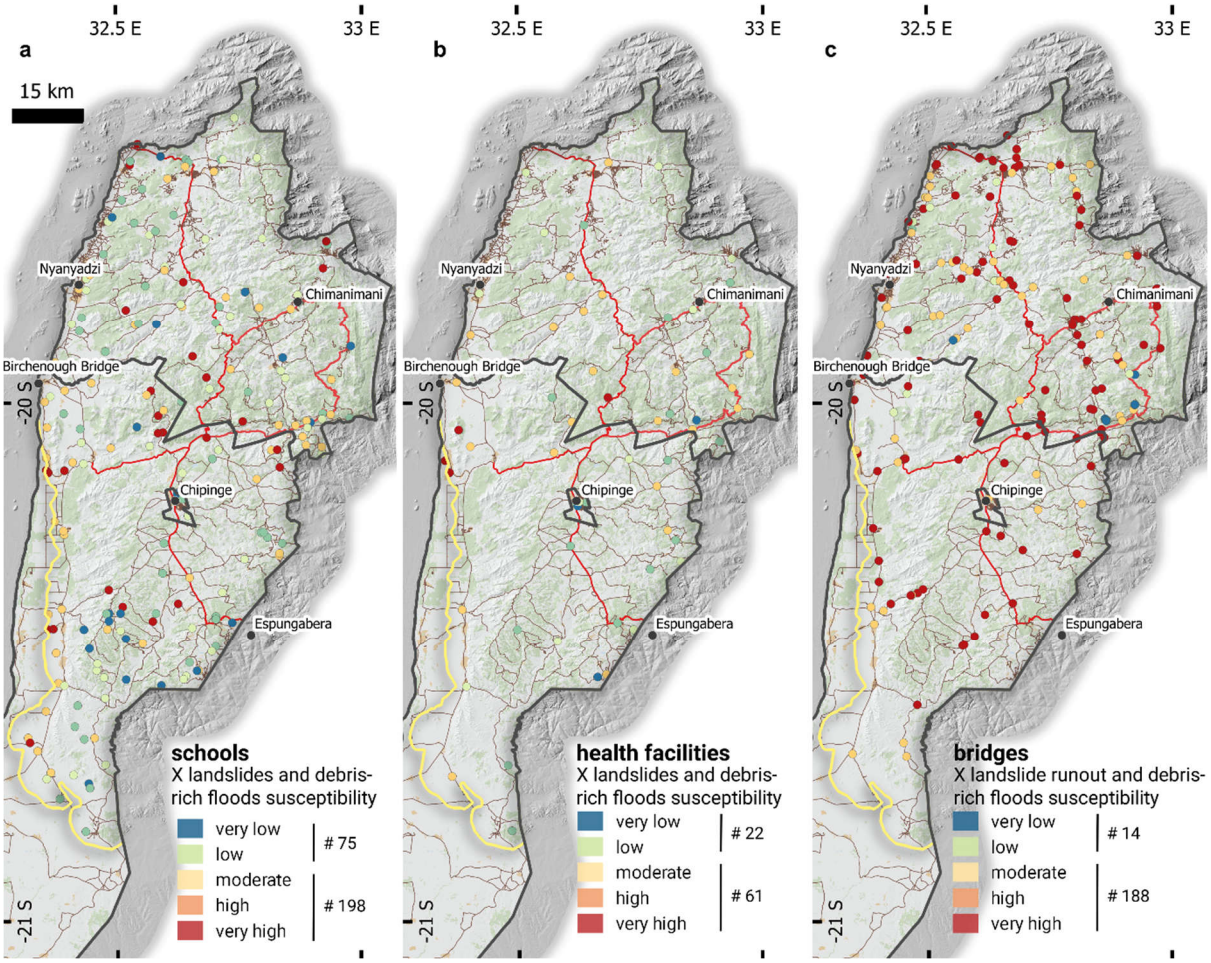

Fig A2. Infrastructure exposure. | **a.** Level of exposure of schools to landslides (source and runout) and debris-rich-floods. **b**. Level of exposure of health facilities to landslides (source and runout) and debris-rich-floods. **c.** Level of exposure of bridges to landslide runouts and debris-rich-floods. The # numbers indicate how many infrastructures are exposed per susceptibility classes. Bridge data © OpenStreetMap contributors 2024. Distributed under the Open Data Commons Open Database License (ODbL) v1.0.

9. References

Amatya, P., Scheip, C., Déprez, A., Malet, J.P., Slaughter, S.L., Handwerger, A.L., Emberson, R., Kirschbaum, D., Jean-Baptiste, J., Huang, M.H., Clark, M.K., Zekkos, D., Huang, J.R., Pacini, F., Boissier, E., 2023. Learnings from rapid response efforts to remotely detect landslides triggered by the August 2021 Nippes earthquake and Tropical Storm Grace in Haiti. Nat. Hazards. https://doi.org/10.1007/s11069-023-06096-6

Arango-Carmona, M.I., Voit, P., Hürlimann, M., Aristizábal, E., Korup, O., 2025. Hillslope-Torrential Hazard Cascades in Tropical Mountains. https://doi.org/10.5194/egusphere-2025-1698

Bennett, G.L., Panici, D., Rengers, F.K., Kean, J.W., Rathburn, S.L., 2025. Landslide-channel feedbacks amplify channel widening during floods. npj Nat. Hazards 2, 7. https://doi.org/10.1038/s44304-025-00059-6

Bhuyan, K., Rana, K., Ozturk, U., Nava, L., Rosi, A., Meena, S.R., Fan, X., Floris, M., van Westen, C., Catani, F., 2025. Towards automatic delineation of landslide source and runout. Eng. Geol. 345, 107866. https://doi.org/10.1016/j.enggeo.2024.107866

Brenna, A., Marchi, L., Borga, M., Zaramella, M., Surian, N., 2023. What drives major channel widening in mountain rivers during floods? The role of debris floods during a high-magnitude event. Geomorphology 430, 108650. https://doi.org/10.1016/j.geomorph.2023.108650

Brenna, A., Surian, N., Ghinassi, M., Marchi, L., 2020. Sediment–water flows in mountain streams: Recognition and classification based on field evidence. Geomorphology 371. https://doi.org/10.1016/j.geomorph.2020.107413

Brenning, A., 2012. Improved Spatial Analysis and Prediction of Landslide Susceptibility: Practical Recommendations, in: Eberhardt, E., Froese, C., Turner, K., Leroueil, S. (Eds.), Landslides and Engineered Slopes: Protecting Society Through Improved Understanding. CRC Press, pp. 789–795.

Broeckx, J., Vanmaercke, M., Duchateau, R., Poesen, J., 2018. A data-based landslide susceptibility map of Africa. Earth-Science Rev. 185, 102–121. https://doi.org/10.1016/j.earscirev.2018.05.002

Chanza, N., Siyongwana, P.Q., Williams-Bruinders, L., Gundu-Jakarasi, V., Mudavanhu, C., Sithole, V.B., Manyani, A., 2020. Closing the Gaps in Disaster Management and Response: Drawing on Local Experiences with Cyclone Idai in Chimanimani, Zimbabwe. Int. J. Disaster Risk Sci. 11, 655–666. https://doi.org/10.1007/s13753-020-00290-x

Chatiza, K., 2019. Cyclone Idai in Zimbabwe - An analysis of policy implications for post-disaster institutional development to strengthen disaster risk management. https://doi.org/10.21201/2019.5273

Church, M., Jakob, M., 2020. What Is a Debris Flood? Water Resour. Res. 56, 1–17. https://doi.org/10.1029/2020WR027144

Croissant, T., Lague, D., Steer, P., Davy, P., 2017. Rapid post-seismic landslide evacuation boosted by dynamic river width. Nat. Geosci. 10, 680–684. https://doi.org/10.1038/ngeo3005

Cutter, S.L., 2018. Compound, Cascading, or Complex Disasters: What's in a Name? Environ. Sci. Policy Sustain. Dev. 60, 16–25. https://doi.org/10.1080/00139157.2018.1517518

Dahal, A., Lombardo, L., 2023. Explainable artificial intelligence in geoscience: a glimpse into the future of landslide susceptibility modeling [Preprint]. Comput. Geosci. 176, 105364. https://doi.org/10.1016/j.cageo.2023.105364

Das, R., Wegmann, K.W., 2022. Evaluation of machine learning-based algorithms for landslide detection across satellite sensors for the 2019 Cyclone Idai event, Chimanimani District, Zimbabwe. Landslides 19, 2965–2981. https://doi.org/10.1007/s10346-022-01912-9

De Angeli, S., Malamud, B.D., Rossi, L., Taylor, F.E., Trasforini, E., Rudari, R., 2022. A multi-hazard framework for spatial-temporal impact analysis. Int. J. Disaster Risk Reduct. 73, 102829. https://doi.org/10.1016/j.ijdrr.2022.102829

de Vilder, S., Kelly, S., Buxton, R., Allan, S., Glassey, P., 2024. Landslide planning guidance reducing landslide risk through land-use planning, GNS Scienc. ed. GNS Science, Lower Hutt. https://doi.org/10.21420/R2X8-FJ49

Depicker, A., Govers, G., Jacobs, L., Campforts, B., Uwihirwe, J., Dewitte, O., 2021a. Interactions between deforestation, landscape rejuvenation, and shallow landslides in the North Tanganyika–Kivu rift region, Africa. Earth Surf. Dyn. 9, 445–462. https://doi.org/10.5194/esurf-9-445-2021

Depicker, A., Jacobs, L., Mboga, N., Smets, B.B., Van Rompaey, A., Lennert, M., Wolff, E., Kervyn, F.F., Michellier, C., Dewitte, O., Govers, G., Rompaey, A. Van, Lennart, M., Kervyn, F.F., Michellier, C., Dewitte, O., Govers, G., 2021b. Historical dynamics of landslide risk from population and forest-cover changes in the Kivu Rift. Nat. Sustain. https://doi.org/10.1038/s41893-021-00757-9

Deprez, A., Marc, O., Malet, J.-P., Stumpf, A., Michéa, D., 2022. ALADIM – A change detection online service for landslide detection from EO imagery, in: EGU General Assembly 2022. Copernicus. https://doi.org/10.5194/egusphere-egu22-3536

Devi, S., 2019. Cyclone Idai : 1 month later , devastation persists. Lancet, World Rep. 393, 1585. https://doi.org/10.1016/S0140-6736(19)30892-X

Dewitte, O., Depicker, A., Moeyersons, J., Dille, A., 2022. Mass Movements in Tropical Climates. Treatise Geomorphol. 338–349. https://doi.org/10.1016/B978-0-12-818234-5.00118-8

Dewitte, O., Dille, A., Depicker, A., Kubwimana, D., Maki Mateso, J.-C., Mugaruka Bibentyo, T., Uwihirwe, J., Monsieurs, E., 2021. Constraining landslide timing in a data-scarce context: from recent to very old processes in the tropical environment of the North Tanganyika-Kivu Rift region. Landslides 18, 161–177. https://doi.org/10.1007/s10346-020-01452-0

Di Napoli, M., Di Martire, D., Bausilio, G., Calcaterra, D., Confuorto, P., Firpo, M., Pepe, G., Cevasco, A., 2021. Rainfall-induced shallow landslide detachment, transit and runout susceptibility mapping by integrating machine learning techniques and gis-based approaches. Water (Switzerland) 13, 11–14. https://doi.org/10.3390/w13040488

Dubey, S., Sattar, A., Goyal, M.K., Allen, S., Frey, H., Haritashya, U.K., Huggel, C., 2023. Mass Movement Hazard and Exposure in the Himalaya. Earth's Futur. 11, 1–18. https://doi.org/10.1029/2022EF003253

Emberson, R., Kirschbaum, D., Stanley, T., 2020. New Global Characterization of Landslide Exposure. Nat. Hazards Earth Syst. Sci. 30, 1–21. https://doi.org/10.5194/nhess-2019-434

Emberson, R., Kirschbaum, D.B., Amatya, P., Tanyas, H., Marc, O., 2022. Insights from the topographic characteristics of a large global catalog of rainfall-induced landslide event inventories. Nat. Hazards Earth Syst. Sci. 22, 1129–1149. https://doi.org/10.5194/nhess-22-1129-2022

Fan, L., Lehmann, P., McArdell, B., Or, D., 2017. Linking rainfall-induced landslides with debris flows runout patterns towards catchment scale hazard assessment. Geomorphology 280, 1–15. https://doi.org/10.1016/j.geomorph.2016.10.007

Fan, X., Juang, C.H., Wasowski, J., Huang, R., Xu, Q., Scaringi, G., van Westen, C.J., Havenith, H.B., 2018. What we have learned from the 2008 Wenchuan Earthquake and its aftermath: A decade of research and challenges. Eng. Geol. 241, 25–32. https://doi.org/10.1016/j.enggeo.2018.05.004

Gill, J.C., Malamud, B.D., 2014. Reviewing and visualizing the interactions of natural hazards. Rev. Geophys. 52, 680–722. https://doi.org/10.1002/2013RG000445

Gill, J.C., Malamud, B.D., Barillas, E.M., Noriega, A.G., 2020. Construction of regional multi-hazard interaction frameworks, with an application to Guatemala. Nat. Hazards Earth Syst. Sci. 20, 149–180. https://doi.org/10.5194/nhess-20-149-2020

Hansen, M.C., Potapov, P. V., Moore, R., Hancher, M., Turubanova, S.A., Tyukavina, A., Thau, D., Stehman, S. V., Goetz, S.J., Loveland, T.R., Kommareddy, A., Egorov, A., Chini, L., Justice, C.O., Townshend, J.R.G., 2013. High-Resolution Global Maps of 21st-Century Forest Cover Change. Science (80-.). 342, 850–853. https://doi.org/10.1126/science.1244693

Highland, L.M., Bobrowsky, P., 2008. The Landslide Handbook — A Guide to Understanding Landslides. Landslides 129.

Hungr, O., Leroueil, S., Picarelli, L., 2014. The Varnes classification of landslide types, an update. Landslides 11, 167–194. https://doi.org/10.1007/s10346-013-0436-y

IFRC, 2020. Zimbabwe: Tropical Cycle Idai - Final Report, International Federation of Red Cross and Red Crescent Societies.

Iverson, R.M., Ouyang, C., 2015. Entrainment of bed material by Earth-surface mass flows: Review and reformulation of depth-integrated theory. Rev. Geophys. 53, 27–58. https://doi.org/10.1002/2013RG000447

Iverson, R.M., Reid, M.E., LaHusen, R.G., 1997. Debris-flow mobilization from landslides. Annu. Rev. Earth Planet. Sci. 25, 85–138.

Iverson, R.M.M., George, D.L.L., Allstadt, K., Reid, M.E.E., Collins, B.D.D., Vallance, J.W., Schilling, S.P., Godt, J.W.W., Cannon, C.M.M., Magirl, C.S.S., Baum, R.L.L., Coe, J. a. A., Schulz, W.H.H., Bower, J.B.B., 2015. Landslide mobility and hazards: Implications of the 2014 Oso disaster. Earth Planet. Sci. Lett. 412, 197–208. https://doi.org/10.1016/j.epsl.2014.12.020

Jacobs, L., Maes, J., Mertens, K., Sekajugo, J., Thiery, W., van Lipzig, N., Poesen, J., Kervyn, M., Dewitte, O., 2016. Reconstruction of a flash flood event through a multi-hazard approach: focus on the Rwenzori Mountains, Uganda. Nat. Hazards 84, 851–876. https://doi.org/10.1007/s11069-016-2458-y

Keck, J., Istanbulluoglu, E., Campforts, B., Tucker, G., Horner-Devine, A., 2024. A landslide runout model for sediment transport, landscape evolution, and hazard assessment applications. Earth Surf. Dyn. 12, 1165–1191. https://doi.org/10.5194/esurf-12-1165-2024

Kritikos, T., Davies, T., 2015. Assessment of rainfall-generated shallow landslide/debris-flow susceptibility and runout using a GIS-based approach: application to western Southern Alps of New Zealand. Landslides 12, 1051–1075. https://doi.org/10.1007/s10346-014-0533-6

Lee, R., White, C.J., Adnan, M.S.G., Douglas, J., Mahecha, M.D., O'Loughlin, F.E., Patelli, E., Ramos, A.M., Roberts, M.J., Martius, O., Tubaldi, E., van den Hurk, B., Ward, P.J., Zscheischler, J., 2024. Reclassifying historical disasters: From single to multi-hazards. Sci. Total Environ. 912, 169120. https://doi.org/10.1016/j.scitotenv.2023.169120

Legros, F., 2002. The mobility of long-runout landslides. Eng. Geol. 63, 301–331. https://doi.org/10.1016/S0013-7952(01)00090-4

Lin, Q., Steger, S., Pittore, M., Zhang, Y., Zhang, J., Zhou, L., Wang, L., Wang, Y., Jiang, T., 2023. Contrasting Population Projections to Induce Divergent Estimates of Landslides Exposure Under Climate Change. Earth's Futur. 11, 1–21. https://doi.org/10.1029/2023EF003741

Maki Mateso, J., Bielders, C.L., Monsieurs, E., Depicker, A., Smets, B., Tambala, T., Bagalwa Mateso, L., Dewitte, O., 2023. Natural and human-induced landslides in a tropical mountainous region: the Rift flanks west of Lake Kivu (DR Congo). Nat. Hazards Earth Syst. Sci. 23, 643–666. https://doi.org/https://doi.org/10.5194/nhess-23-643-2023

Marc, O., Hovius, N., 2015. Amalgamation in landslide maps: Effects and automatic detection. Nat. Hazards Earth Syst. Sci. 15, 723–733. https://doi.org/10.5194/nhess-15-723-2015

Marc, O., Stumpf, A., Malet, J.P., Gosset, M., Uchida, T., Chiang, S.H., 2018. Initial insights from a global database of rainfall-induced landslide inventories: The weak influence of slope and strong influence of total storm rainfall. Earth Surf. Dyn. 6, 903–922. https://doi.org/10.5194/esurf-6-903-2018

McGuire, L.A., Ebel, B.A., Rengers, F.K., Vieira, D.C.S., Nyman, P., 2024. Fire effects on geomorphic processes. Nat. Rev. Earth Environ. 41–79. https://doi.org/10.1038/s43017-024-00557-7

Melo, R., Zêzere, J.L., Rocha, J., Oliveira, S.C., 2019. Combining data-driven models to assess susceptibility of shallow slides failure and run-out. Landslides 16, 2259–2276. https://doi.org/10.1007/s10346-019-01235-2

Merghadi, A., Yunus, A.P., Dou, J., Whiteley, J., ThaiPham, B., Bui, D.T., Avtar, R., Abderrahmane, B., 2020. Machine learning methods for landslide susceptibility studies: A comparative overview of algorithm performance. Earth-Science Rev. 207, 103225.

https://doi.org/10.1016/j.earscirev.2020.103225

Mergili, M., Emmer, A., Juřicová, A., Cochachin, A., Fischer, J.T., Huggel, C., Pudasaini, S.P., 2018. How well can we simulate complex hydro-geomorphic process chains? The 2012 multi-lake outburst flood in the Santa Cruz Valley (Cordillera Blanca, Perú). Earth Surf. Process. Landforms 43, 1373–1389. https://doi.org/10.1002/esp.4318

Mergili, M., Schwarz, L., Kociu, A., 2019. Combining release and runout in statistical landslide susceptibility modeling. Landslides 16, 2151–2165. https://doi.org/10.1007/s10346-019-01222-7

Merz, B., Blöschl, G., Vorogushyn, S., Dottori, F., Aerts, J.C.J.H., Bates, P., Bertola, M., Kemter, M., Kreibich, H., Lall, U., Macdonald, E., 2021. Causes, impacts and patterns of disastrous river floods. Nat. Rev. Earth Environ. 2, 592–609. https://doi.org/10.1038/s43017-021-00195-3

Milledge, D.G., Densmore, A.L., Bellugi, D., Rosser, N.J., Watt, J., Li, G., Oven, K.J., 2019. Simple rules to minimise exposure to coseismic landslide hazard. Nat. Hazards Earth Syst. Sci. 19, 837–856. https://doi.org/10.5194/nhess-19-837-2019

Nohrstedt, D., Mazzoleni, M., Parker, C.F., Di Baldassarre, G., 2021. Exposure to natural hazard events unassociated with policy change for improved disaster risk reduction. Nat. Commun. 12. https://doi.org/10.1038/s41467-020-20435-2

Pedregosa, F., Varoquaux, G., Gramfort, A., Michel, V., Thirion, B., Grisel, O., Blondel, M., Prettenhofer, P., Weiss, R., Dubourg, V., Vanderplas, J., 2011. Scikit-learn: Machine Learning in Python. J. Mach. Learn. Res. 1, 2815–2830.

Pudasaini, S.P., Krautblatter, M., 2021. The mechanics of landslide mobility with erosion. Nat. Commun. 12. https://doi.org/10.1038/s41467-021-26959-5

Reichenbach, P., Rossi, M., Malamud, B.D., Mihir, M., Guzzetti, F., 2018. A review of statistically-based landslide susceptibility models. Earth-Science Rev. 180, 60–91. https://doi.org/10.1016/j.earscirev.2018.03.001

Roback, K., Clark, M.K., West, A.J., Zekkos, D., Li, G., Gallen, S.F., Chamlagain, D., Godt, J.W., 2018. The size, distribution, and mobility of landslides caused by the 2015 Mw7.8 Gorkha earthquake, Nepal. Geomorphology 301, 121–138. https://doi.org/10.1016/j.geomorph.2017.01.030

Scheip, C.M., Wegmann, K.W., 2021. HazMapper: A global open-source natural hazard mapping application in Google Earth Engine. Nat. Hazards Earth Syst. Sci. 21, 1495–1511. https://doi.org/10.5194/nhess-21-1495-2021

Sekajugo, J., Kagoro-Rugunda, G., Mutyebere, R., Kabaseke, C., Mubiru, D., Kanyiginya, V., Vranken, L., Jacobs, L., Dewitte, O., Kervyn, M., 2024. Exposure and physical vulnerability to geo-hydrological hazards in rural environments: A field-based assessment in East Africa. Int. J. Disaster Risk Reduct. 102, 104282. https://doi.org/10.1016/j.ijdrr.2024.104282

Sharma, S., Talchabhadel, R., Nepal, S., Ghimire, G.R., Rakhal, B., Panthi, J., Adhikari, B.R., Pradhanang, S.M., Maskey, S., Kumar, S., 2023. Increasing risk of cascading hazards in the central Himalayas. Nat. Hazards 119, 1117–1126. https://doi.org/10.1007/s11069-022-05462-0

Sirko, W., Kashubin, S., Ritter, M., Annkah, A., Bouchareb, Y.S.E., Dauphin, Y., Keysers, D., Neumann, M., Cisse, M., Quinn, J., 2021. Continental-Scale Building Detection from High Resolution Satellite Imagery 1–15.

Slater, L.J., Singer, M.B., Kirchner, J.W., 2015. Hydrologic versus geomorphic drivers of trends in flood hazard. Geophys. Res. Lett. 42, 370–376. https://doi.org/10.1002/2014GL062482

Stanley, T., Kirschbaum, D.B., 2017. A heuristic approach to global landslide susceptibility mapping. Nat. Hazards 87, 145–164. https://doi.org/10.1007/s11069-017-2757-y

Tanyaş, H., van Westen, C.J., Allstadt, K.E., Anna Nowicki Jessee, M., Görüm, T., Jibson, R.W., Godt, J.W., Sato, H.P., Schmitt, R.G., Marc, O., Hovius, N., 2017. Presentation and Analysis of a Worldwide Database of Earthquake-Induced Landslide Inventories. J. Geophys. Res. Earth Surf. 122, 1991–2015. https://doi.org/10.1002/2017JF004236

Tiecke, T.G., Liu, X., Zhang, A., Gros, A., Li, N., Yetman, G., Kilic, T., Murray, S., Blankespoor, B., Prydz, E.B., Dang, H.-A.H., 2017. Mapping the World Population One Building at a Time. Mapp. World Popul. One Build. a Time. https://doi.org/10.1596/33700

Tilloy, A., Malamud, B.D., Winter, H., Joly-Laugel, A., 2019. A review of quantification methodologies for multi-hazard interrelationships. Earth-Science Rev. 196, 102881. https://doi.org/10.1016/j.earscirev.2019.102881

UNESCO Intergovernmental Hydrological Program, 2021. Comprehensive resilience building in the Chimanimani and Chipinge Districts. Paris, France.

Van Den Bout, B., Tang, C., Van Westen, C., Jetten, V., 2022. Physically based modeling of co-seismic landslide, debris flow, and flood cascade. Nat. Hazards Earth Syst. Sci. 22, 3183–3209. https://doi.org/10.5194/nhess-22-3183-2022

van Westen, C.J., Van Asch, T.W.J.J., Soeters, R., 2006. Landslide hazard and risk zonation—why is it still so difficult? Bull. Eng. Geol. Environ. 65, 167–184. https://doi.org/10.1007/s10064-005-0023-0

Vanmaercke, M., Chen, Y., Haregeweyn, N., De Geeter, S., Campforts, B., Heyndrickx, W., Tsunekawa, A., Poesen, J., 2020. Predicting gully densities at sub-continental scales: a case study for the Horn of Africa. Earth Surf. Process. Landforms 45, 3763–3779. https://doi.org/10.1002/esp.4999

Wallace, C.S., Santi, P.M., Walton, G., 2022. Scoring system to predict landslide runout in the Pacific Northwest, USA. Landslides 19, 1449–1461. https://doi.org/10.1007/s10346-021-01839-7

Weiss, A., 2001. Topographic position and landforms analysis, in: ESRI User Conference. San Diego, CA, pp. 227–245.

Wohl, E., Brierley, G., Cadol, D., Coulthard, T.J., Covino, T., Fryirs, K.A., Grant, G., Hilton, R.G., Lane, S.N., Magilligan, F.J., Meitzen, K.M., Passalacqua, P., Poeppl, R.E., Rathburn, S.L., Sklar, L.S., 2019. Connectivity as an emergent property of geomorphic systems. Earth Surf. Process. Landforms 44, 4–26. https://doi.org/10.1002/esp.4434

Yanites, B.J., Clark, M.K., Roering, J.J., West, A.J., Zekkos, D., Baldwin, J.W., Cerovski-Darriau, C., Gallen, S.F., Horton, D.E., Kirby, E., Leshchinsky, B.A., Mason, H.B., Moon, S., Barnhart, K.R., Booth, A., Czuba, J.A., McCoy, S., McGuire, L., Pfeiffer, A., Pierce, J., 2025. Cascading land surface hazards as a nexus in the Earth system. Science (80-.). 388. https://doi.org/10.1126/science.adp9559

Zêzere, J.L., Pereira, S., Melo, R., Oliveira, S.C., Garcia, R.A.C., 2017. Mapping landslide susceptibility using data-driven methods. Sci. Total Environ. 589, 250–267. https://doi.org/10.1016/j.scitotenv.2017.02.188

Zhou, W., Qiu, H., Wang, L., Pei, Y., Tang, B., Ma, S., Yang, D., Cao, M., 2022. Combining rainfall-induced shallow landslides and subsequent debris flows for hazard chain prediction. Catena 213, 106199. https://doi.org/10.1016/j.catena.2022.106199

Zimbabwe National Statistics Agency, 2022. Population and housing census 2022.